Intrinsic variation of the polarization-resolved SHG from collagen: Multiscale analysis and application to parchments

Giulia Galante, Laurianne Robinet, Sylvie Heu-Thao, Clément Caporal, Gaël Latour, Marie-Claire Schanne-Klein

Intrinsic variation of the polarization-resolved SHG from collagen: multiscale analysis and application to parchments

Giulia Galante,[1] Laurianne Robinet,[2] Sylvie Heu-Thao,[2] Clément Caporal,[1] Gaël Latour,[1,3] and Marie-Claire Schanne-Klein[1,a)]

[1)] *Laboratoire d'Optique et Biosciences, CNRS, Inserm, Ecole polytechnique, Institut Polytechnique de Paris, 91128 Palaiseau, France*

[2)] *Centre de Recherche sur la Conservation (CRC), Muséum national d'Histoire naturelle, Ministère de la Culture, CNRS, 75005 Paris, France*

[3)] *Université Paris-Saclay, 91190 Gif-sur-Yvette, France*

(Dated: 7 March 2025)

Second harmonic generation (SHG) microscopy is nowadays the gold standard technique for collagen structural imaging in intact tissues with sub-micrometer resolution. This multiphoton modality can be combined with polarimetry to provide key information about the 3D hierarchical organization of collagen. Notably, the so-called anisotropy parameter processed from polarization-resolved SHG (P-SHG) has been shown to vary with the orientational disorder of the fibrils within the focal volume and with their out-of-plane orientation. However, analytical equations describing both effects within the same formalism are still lacking. In this work, we present a unified multiscale theoretical approach of the intrinsic variations of the anisotropy parameter. We then measure these variations in the very same collagen samples to ensure reliable comparisons. To that end, we use parchments, which are materials made from animal skins and which contain almost exclusively collagen. These parchments are manufactured in different ways to obtain different collagen distributions. Our series of measurements exhibit a good agreement with our theoretical approach, which shows the relevance of P-SHG measurements to probe collagen multiscale organization in tissues.

[a)] Electronic mail: marie-claire.schanne-klein@polytechnique.edu

I. INTRODUCTION

Collagen is a major structural protein in mammals[1]. It is found in many organs such as skin, tendons, arteries, bones, cornea, etc... and as such is involved in many pathologies. There are many collagen types, which are all characterized by triple helical domains composed of three α chains at the molecular scale (Fig. 1.a). In collagen fibrillar types, these triple helices align to form fibrils with diameters ranging between 10 nm and 300 nm. Fibrils can further organize in various ways, most usually in fibers that are tight assemblies of aligned fibrils[1]. This so-called hierarchical organization of collagen is specific to each tissue and crucial for its biological function. Collagen remodeling in the course of pathologies such as fibrosis or cancer may affect this three-dimensional (3D) organization and impede the tissue function. Accurate multiscale characterization of collagen distribution in tissues is therefore a major biomedical issue.

Second harmonic generation (SHG) microscopy is nowadays the gold standard technique for collagen structural imaging with sub-micrometer resolution[2]. As SHG is a coherent multiphoton process specific for dense and non-centrosymmetric materials, it provides three dimensional (3D) imaging of fibrillar collagen without any staining and with unequaled specificity and sensitivity[3]. Moreover, it can be combined with other multiphoton modalities, notably two-photon excited fluorescence (2PEF), to provide multimodal 3D images of thick collagen-rich tissues[2].

Polarization-resolved SHG microscopy (P-SHG) has been shown to provide more accurate information about collagen distribution in tissues[4–16]. P-SHG consists in recording series of SHG images for different orientations of the linear polarization of the incident laser excitation. A polarimetric diagram is thus measured in every voxel and its main axis provides the mean direction of the collagen fibrils within this voxel. The so-called anisotropy parameter, which is noted ρ (or alternatively γ), is also of great interest for collagen structural imaging: it is defined as the ratio of the SHG signal measured for an incident polarization parallel to the collagen fibrils to that for an incident polarization perpendicular to these fibrils. This anisotropy parameter has been shown to be directly related to the pitch of the collagen triple helix[5,17].

However, P-SHG measurement of the anisotropy parameter is a complex issue and has been shown to be affected by several experimental artifacts. First, collagen-rich tissues can

exhibit birefringence and diattenuation that distort the incoming polarization and affect the polarimetric diagrams in depth[4,6,7,18,19]. Second, high focusing scrambles polarizations, which affects the polarimetric diagrams in a different way for forward versus backward SHG detection[20]. Third, these measurements can also be affected by the noise background[21,22]. Fortunately, all these experimental artifacts have been extensively studied and can be either corrected or at least estimated to provide reliable error bars.

Besides these experimental measurement issues, the anisotropy parameter also exhibit intrinsic variations due to the variety of collagen hierarchical organizations in tissues. P-SHG microscopy probes this multiscale three-dimensional (3D) structure at the optical scale, within the focal volume (usually around 1 μm^3) that may contain several fibrils with different directions. The anisotropy parameter has been shown to vary with the orientational disorder of these fibrils[5,8–10,13,16] and with their out-of-plane orientation[11–16]. Both effects have been described theoretically, but tractable analytical equations describing both effects within the same formalism are still lacking. Moreover, these effects have been evidenced experimentally in different samples, which is prone to experimental artifacts.

In this work, we present a unified multiscale theoretical approach of the intrinsic variations of the anisotropy parameter measured in collagen using P-SHG microscopy. We then measure these variations in the very same collagen samples to get rid of experimental artifacts affecting the P-SHG measures. To that end, we use parchments, which are animals skin that are preserved by liming, scraping, and drying under tension[23]. Parchments thus contain almost solely collagen. Due to the last manufacturing step, the collagen fibers are stretched and well aligned parallel to the parchment surface, that is in the imaging plane[24]. However, a different finishing treatment can result in the presence of out-of-plane fibrils at the surface of some limited region of the same parchment. In the same way, artificial aging by heat for different durations of samples from the same parchment can induce increasing levels of disorder in the fibrillar structure. Our series of measurements in these parchments exhibit a good agreement with our theoretical approach and show the relevance of these P-SHG measurements of collagen multiscale organization in tissues.

II. ANALYTICAL THEORY OF SHG SIGNAL FROM FIBRILLAR COLLAGEN

A. A multiscale approach

Second harmonic generation from fibrillar collagen has been shown to originate from the peptide bonds at molecular level[3,5,17,25]. These peptide bonds exhibit delocalized π electrons between electro-donor (N) and electro-acceptor (O) groups that provide a non centrosymmetric environment. The induced dipole thus exhibits a second-order nonlinear optical response characterized by a so-called hyperpolarizability tensor $\underline{\underline{\beta}}$:

$$\underline{p} = \underline{\underline{\beta}}\ \underline{E}.\underline{E} \tag{1}$$

Here $\underline{E}$ is the complex amplitude of the incident electric field: $\underline{E}(t) = \underline{E}\ e^{-i\omega t} + cc$, and the dependence on the position $\underline{r}$ has been dropped for simplicity.

On a larger scale, up to the optical scale, all these dipoles sum up to build a polarization $\underline{P}$, which acts as a source term for the second harmonic signal:

$$\underline{P} = \sum \underline{p} = \epsilon_0\ \underline{\underline{\chi}}^{(2)}\ \underline{E}.\underline{E} \tag{2}$$

The susceptibility tensor $\chi^{(2)}$ is thus obtained as the summation of all hyperpolarizability tensors within a unit volume. Equally, it means that the SHG signal measured in a multi-photon microscope is obtained as the coherent summation of all SH electric fields radiated by the elementary nonlinear dipoles of each peptide bond within the focal volume.

Importantly, collagen exhibits a hierarchical organization from the α chain to the triple helix, the fibril and the assembly of fibrils as depicted in Fig. 1.a. Due to this multiscale structure, the summation of the hyperpolarizability tensors must be considered on two increasing scales:

- On the sub-micrometer scale that corresponds to the α chain, the triple helix or the fibril. On this scale, all the peptides bonds have the same polarity, so that the coherent summation of their contributions results in constructive interferences.

- On the micrometer scale, that is the optical scale of the focal volume. On this scale, there are multiple fibrils with various 3D orientations, including opposite polarities, which can lead to partially destructive interferences. The resulting polarization thus

depends on the precise spatial distribution of the collagen fibrils within the focal volume, which is specific to each tissue. Furthermore, this assembly of fibrils may have different orientations with respect to the light propagation axis Z of the microscope.

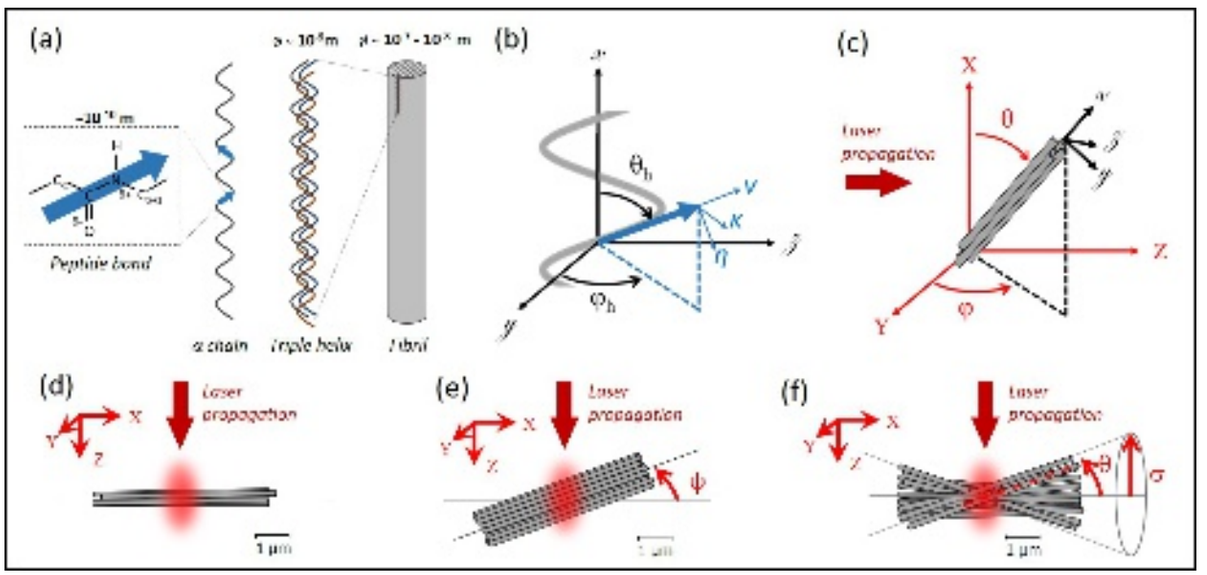

FIG. 1. Multiscale structure of collagen. (a) The collagen triple helix is composed of 3 superwound α chains. These triple helices self-assemble to form fibrils with diameter ranging from $\approx 10\ nm$ to $300\ nm$. The elementary sources of SHG signal are the peptide bonds along the α chains. (b) In the frame of the α chain, the pitch angle θ_h is defined as the orientation of the peptide bond to the triple helix axis. (c) Euler angles θ and φ parametrizing the transformation from the fibril frame (x, y, z) to the laboratory frame (X, Y, Z). The red arrow represents the propagation axis of the excitation laser. (d) Assembly of in-plane fibrils. The red spot represents the focal volume. (e) Assembly of aligned out-of-plane fibrils. The out-of-plane angle is defined as ψ. (f) Assembly of disordered fibrils in the imaging plane. The disorder of the fibril distribution $p(\theta)$ increases when the variance σ increases.

In many tissues such as skin and tendon, fibrils assemble to form fibers that can be considered as tight assemblies of aligned fibrils[1]. Because parchments are made from animal skin composed of collagen fibers, SHG microscopy probes these fibers at the micrometer scale. Whatever the scale under consideration, the collagen susceptibility tensor $\chi^{(2)}$ is calculated from the peptide bond hyperpolarizability β in two steps:

- Changing the frame of reference from the peptide bond frame to the α chain/triple

helix/fibril frame or from the fibril frame to the laboratory frame

- Summation over all the peptide bonds within the α chain/triple helix/fibril or over all fibrils within the focal volume

B. From the peptide bond to the fibril scale

Let's first calculate the susceptibility of a collagen α chain, triple helix or fibril composed of N_{pb} peptide bonds par unit volume. As usually assumed[3,5,17,25], we consider here that only one component $\beta_{\nu\nu\nu}$ of the hyperpolarizability tensor contributes to the SHG signal, ν standing for the peptide bond direction. The usual formula for tensor summation is then simplified as follows:

$$\chi^{(2)}_{ijk} = \frac{1}{\epsilon_0} \sum_n T_{n,i\nu}\, T_{n,j\nu}\, T_{n,k\nu}\, \beta_{\nu\nu\nu} \tag{3}$$

Here n is the peptide bond number and T_n is the transformation matrix between the peptide bond frame and the frame of the α chain, triple helix or fibril, which is parameterized by Euler angles (Fig. 1.b). The α chain is characterized by a pitch angle θ_h, so that all peptides bonds have the same nutation angle θ_h to the axis of the α chain and a random precession angle φ_h around this axis. As usually assumed[5,17,25], we neglect the slight orientation dispersion introduced by the triple helical structure, so that the same Euler angles can be used at the triple helix scale. We make the same assumption at the fibril scale and assume that all triple helices are perfectly parallel along the fibril. Therefore, the same Euler angles are used on the α chain, triple helix and fibril scales.

Furthermore, these structures exhibit a cylindrical symmetry, so that we expect only four independent tensor components: $\chi^{(2)}_{xxx}$, $\chi^{(2)}_{xyy} = \chi^{(2)}_{xzz}$, $\chi^{(2)}_{yyx} = \chi^{(2)}_{yxy} = \chi^{(2)}_{zzx} = \chi^{(2)}_{zxz}$ (achiral) and $\chi^{(2)}_{yzx} = \chi^{(2)}_{yxz} = -\chi^{(2)}_{zyx} = -\chi^{(2)}_{zxy}$ (chiral), where x is the axis of the α chain, triple helix or fibril. Using Eq. 3, we obtain only 2 nonzero independent components:

$$\begin{aligned}
\chi^{(2)}_{xxx} &= \frac{1}{\epsilon_0} \sum_n T^3_{n,x\nu}\, \beta_{\nu\nu\nu} \\
\chi^{(2)}_{xyy} &= \chi^{(2)}_{yyx} = \frac{1}{\epsilon_0} \sum_n T_{n,x\nu}\, T^2_{n,y\nu}\, \beta_{\nu\nu\nu} \\
\chi^{(2)}_{yzx} &= \chi^{(2)}_{zyx} = 0
\end{aligned} \tag{4}$$

Thus,

$$\begin{aligned}\chi^{(2)}_{xxx} &= \frac{N_{pb}}{\epsilon_0}\ \cos^3\theta_h\ \beta_{\nu\nu\nu} \\ \chi^{(2)}_{xyy} = \chi^{(2)}_{yyx} &= \frac{N_{pb}}{\epsilon_0}\ \cos\theta_h\ \sin^2\theta_h\ <\cos^2\varphi_h>\ \beta_{\nu\nu\nu} = \frac{N_{pb}}{2\ \epsilon_0}\ \cos\theta_h\ \sin^2\theta_h\ \beta_{\nu\nu\nu}\end{aligned} \tag{5}$$

The anisotropy parameter ρ_{fib} is then defined as the ratio of these two components and can be expressed as a function of the pitch angle θ_h of the triple helix:

$$\rho_{\text{fib}} = \frac{\chi^{(2)}_{xxx}}{\chi^{(2)}_{xyy}} = \frac{2\cos^2\theta_h}{\sin^2\theta_h} = \frac{2}{\tan^2\theta_h} \tag{6}$$

This anisotropy parameter ρ_{fib} is thus a constant characterizing the collagen triple helical structure.

C. From the fibril scale to the optical scale

1. Frame transformation

There are usually several fibrils within the focal volume on the micrometer scale. They are parameterized by their Euler angles θ and φ in the laboratory frame (X, Y, Z), where Z is the laser propagation axis in the microscope (Fig. 1.c). The transformation matrix T is:

$$T(\theta,\varphi) = \begin{bmatrix} \cos\theta & -\sin\theta & 0 \\ \cos\varphi\sin\theta & \cos\varphi\cos\theta & -\sin\varphi \\ \sin\varphi\sin\theta & \sin\varphi\cos\theta & \cos\varphi \end{bmatrix} \tag{7}$$

The susceptibility tensor components on the optical scale are then written:

$$\chi^{(2)}_{IJK} = \sum_{ijk} \iint p(\theta,\varphi)\ T_{Ii}(\theta,\varphi)\ T_{Jj}(\theta,\varphi)\ T_{Kk}(\theta,\varphi)\ \chi^{(2)}_{ijk}\ d\theta\ d\varphi \tag{8}$$

Here $p(\theta,\varphi)$ is the probability of the fibril orientation (θ,φ) within the focal volume. For the sake of simplicity, we consider identical fibrils (same diameter) and a constant total volume density. This assembly of fibrils may have any type of symmetry, so that there are usually more tensor components than on the fibril scale. However, we assume here that the plane wave approximation is valid because we use an air objective lens with a low numerical aperture (NA=0.5). As a consequence, the susceptibility components with

a Z coordinate are not used to calculate the SHG signal, so we only need to calculate the following components:

$$\begin{aligned}
\chi^{(2)}_{XXX} &= \iint p(\theta,\varphi)\left(\cos^3\theta\ \chi^{(2)}_{xxx} + 3\ \cos\theta\sin^2\theta\ \chi^{(2)}_{xyy}\right)\ d\theta\ d\varphi \\
\chi^{(2)}_{XYY} = \chi^{(2)}_{YXY} = \chi^{(2)}_{YYX} &= \iint p(\theta,\varphi)\ \Big(\cos\theta\sin^2\theta\cos^2\varphi\ \chi^{(2)}_{xxx} \\
&\quad + \left[\cos^3\theta\cos^2\varphi + \cos\theta\sin^2\varphi - 2\ \cos\theta\ \sin^2\theta\cos^2\varphi\right]\ \chi^{(2)}_{xyy}\ \Big)\ d\theta\ d\varphi \\
\chi^{(2)}_{XXY} = \chi^{(2)}_{YXX} = \chi^{(2)}_{XYX} &= \iint p(\theta,\varphi)\ \Big(\cos^2\theta\sin\theta\cos\varphi\ \chi^{(2)}_{xxx} \\
&\quad + \left[\sin^3\theta\cos\varphi - 2\ \cos^2\theta\ \sin\theta\cos\varphi\right]\ \chi^{(2)}_{xyy}\ \Big)\ d\theta\ d\varphi \\
\chi^{(2)}_{YYY} &= \iint p(\theta,\varphi)\left(\sin^3\theta\ \cos^3\varphi\ \chi^{(2)}_{xxx} + 3\ \cos^2\theta\ \sin\theta\ \cos^3\varphi\ \chi^{(2)}_{xyy}\right)\ d\theta\ d\varphi
\end{aligned} \tag{9}$$

Note that this calculation can be generalised to the strong focusing regime, beyond the plane wave approximation[19,20]. In this regime, numerical calculations based on the Green functions formalism have to take into account the tensor components with a Z coordinate, which calculation is similar to Eq. 9.

We now consider specific fibril assemblies that correspond to common geometries in tissues. The aim is to simplify Eq. 9 to gain insight into the effect of multiscale collagen organization on the P-SHG signal.

2. Assembly of aligned in-plane fibrils

Let's first consider the basic case of collagen fibrils all aligned together within the imaging plane, such as fibers in stretched tendons or fibrils in corneal lamellae[8,20] (Fig. 1.d). In parchments, it corresponds to fibers (tight assembly of aligned fibrils) within the parchment plane. This geometry corresponds to $\theta = 0$ and $\varphi = 0$, which greatly simplifies Eq. 9:

$$\begin{aligned}
\chi^{(2)}_{XXX} &= \chi^{(2)}_{xxx} \\
\chi^{(2)}_{XYY} = \chi^{(2)}_{YXY} &= \chi^{(2)}_{YYX} = \chi^{(2)}_{xyy} \\
\chi^{(2)}_{XXY} = \chi^{(2)}_{YXX} &= \chi^{(2)}_{XYX} = \chi^{(2)}_{YYY} = 0
\end{aligned} \tag{10}$$

The anisotropy parameter on the optical scale measured for this in-plane aligned assembly ρ^{in}_{opt} is therefore equal to the one on the fibril scale:

$$\rho^{in}_{\text{opt}} = \frac{\chi^{(2)}_{XXX}}{\chi^{(2)}_{XYY}} = \rho_{\text{fib}}. \tag{11}$$

P-SHG imaging of collagen samples exhibiting well-aligned fibrils in the imaging plane thus provides a measure of ρ_{fib}. Such measurements have been reported in stretched tendons and corneal lamellae and give values of 1.36 and 1.45 respectively[8,20]. This corresponds to a pitch angle of around 50°, close to the pitch angle of 45° measured by X-rays diffraction[26]. The difference is attributed to mainly three effects: (i) the nonlinear dipole may be not perfectly aligned along the peptide bond, as shown by quantum-chemistry simulations[27–29]; (ii) the pitch angle may vary with the hydration state of collagen[30]; (iii) the triple helical structure leads to a dispersion of the peptide bond angles to the main axis. Moreover, fibrils can exhibit a super-coiled structure that also leads to a dispersion of the peptide bond angles[31,32]. These effects can be taken into account by a more complex calculation and provides a better agreement with the collagen structure[5,13,33].

3. Assembly of aligned out-of-plane fibrils

Now let's consider an assembly of well-aligned fibrils with an out-of-plane angle of ψ relative to the imaging plane (Fig. 1.e). In parchments, it corresponds to fibers pointing out of the parchment plane. This geometry corresponds to $\theta = \psi$ and $\varphi = -\frac{\pi}{2}$ and Eq. 9 is simplified as follows:

$$\begin{aligned}
\chi^{(2)}_{XXX} &= \cos^3\psi\ \chi^{(2)}_{xxx} + 3\ \cos\psi\ \sin^2\psi\ \chi^{(2)}_{xyy} \\
\chi^{(2)}_{XYY} &= \chi^{(2)}_{YXY} = \chi^{(2)}_{YYX} = \cos\psi\ \chi^{(2)}_{xyy} \\
\chi^{(2)}_{XXY} &= \chi^{(2)}_{YXX} = \chi^{(2)}_{XYX} = \chi^{(2)}_{YYY} = 0
\end{aligned} \tag{12}$$

The anisotropy parameter on the optical scale for this out-of-plane geometry ρ^{out}_{opt} is then written as:

$$\rho^{out}_{\text{opt}} = \frac{\chi^{(2)}_{XXX}}{\chi^{(2)}_{XYY}} = \rho_{\text{fib}}\ \cos^2\psi\ +\ 3\ \sin^2\psi \tag{13}$$

It increases from ρ_{fib} to 3 as the out-of-plane angle ψ increases from 0 to $\frac{\pi}{2}$[4,11,12].

4. Assembly of disordered fibrils in the imaging plane

Finally, let's consider a disordered assembly of fibrils, with an dispersion $p(\theta)$ of the nutation angle and a random precession angle φ with respect to the axis X (Fig. 1.f)[8]. In this case, the cylindrical symmetry is preserved in the (X, Y, Z) frame. Taking advantage of

$< \cos^2\varphi >=< \sin^2\varphi >= 1/2$ and $< \cos^3\varphi >=< \cos\varphi >= 0$, one obtains from Eq. 9:

$$\begin{aligned}
\chi^{(2)}_{XXX} &= \int p(\theta)\left(\cos^3\theta\ \chi^{(2)}_{xxx} + 3\ \cos\theta\sin^2\theta\ \chi^{(2)}_{xyy}\right) d\theta \\
\chi^{(2)}_{XYY} &= \chi^{(2)}_{YXY} = \chi^{(2)}_{YYX} = \frac{1}{2}\int p(\theta)\left(\cos\theta\sin^2\theta\ \chi^{(2)}_{xxx} + \left[3\cos^3\theta - \cos\theta\right]\ \chi^{(2)}_{xyy}\ \right) d\theta \\
\chi^{(2)}_{XXY} &= \chi^{(2)}_{YXX} = \chi^{(2)}_{XYX} = \chi^{(2)}_{YYY} = 0
\end{aligned} \tag{14}$$

The anisotropy parameter on the optical scale for this disordered in-plane assembly ρ^{dis}_{opt} is then written as:

$$\rho^{dis}_{\text{opt}} = \frac{\chi^{(2)}_{XXX}}{\chi^{(2)}_{XYY}} = \frac{2\rho_{\text{fib}}\left\langle\cos^3\theta\right\rangle + \ 6\ \left\langle\cos\theta\sin^2\theta\right\rangle}{\rho_{\text{fib}}\left\langle\cos\theta\sin^2\theta\right\rangle + 3\left\langle\cos^3\theta\right\rangle - \left\langle\cos\theta\right\rangle} \tag{15}$$

where <> stands for the averaging over the θ distribution. Numerical calculation of Eq. 15 thus necessitates to define the distribution $p(\theta)$. First, for simplicity, we assume a Gaussian distribution $g(\theta) = \frac{1}{\sigma\sqrt{2\pi}} exp(-\frac{\theta^2}{2\sigma^2})$ and consider that the disorder increases when the Gaussian variance σ increases[8]. Second, we use a Van Mises distribution, which is better suited for an angular distribution: $V(\theta) = \frac{1}{2\pi I_0(\kappa)} exp(\kappa cos(\theta))$, where $I_0(\kappa)$ is the zero-order modified Bessel function and κ is the concentration. The latter parameter is analogous to $1/\sigma^2$ for a Gaussian distribution, so that the disorder is considered to increase with $1/\sqrt{(\kappa)} \approx \sigma$. As expected, the two calculations give very similar results: ρ^{dis}_{opt} increases from ρ_{fib} to around 2.5 when the disorder increases (see section $IV.C$ below).

This calculation also applies to a disordered assembly of collagen triple helices within a single fibril within the focal volume, that is a partial loss of the fibril structure.

D. Polarization-resolved SHG signal

The SHG signal I_{SHG} is obtained as the squared modulus of the nonlinear polarization $\underline{P}$ introduced in Eq. 2. No polarization analysis of this signal is performed in our experimental setup because of backward detection, so we have to sum the X and Y contributions:

$$I_{SHG} \propto \left|\sum_{J,K} \chi^{(2)}_{XJK}\ E_J\ E_K\right|^2 \ + \ \left|\sum_{J,K} \chi^{(2)}_{YJK}\ E_J\ E_K\right|^2 \tag{16}$$

I_{SHG} then varies with the polarization orientation α of the linearly-polarized incident

field:

$$\underline{E} = E_0\, e^{ikZ} \begin{pmatrix} \cos\alpha \\ \sin\alpha \\ 0 \end{pmatrix}_{(X_0,Y_0,Z)} \tag{17}$$

We have introduced the stage frame (X_0, Y_0, Z), where X_0 is the reference axis for the incident linear polarization in the microscope and corresponds to the X_0 axis of the microscope stage and of the laser scanning direction (Fig. 2.b). It can be different from the axis X that is attached to the collagen sample and corresponds to the direction of the fibril assembly in the imaging plane (Fig 1). We thus introduce the angle $\alpha_0 = \widehat{X_0X}$ (Fig. 2.b).

As mentioned above, the susceptibility tensor on the optical scale does not always exhibit a cylindrical symmetry. However, in all the examples described in subsection *II.C*, there are only two independent non-zero components as in cylindrical symmetry: $\chi^{(2)}_{XXX}$ and $\chi^{(2)}_{XYY} = \chi^{(2)}_{YXY} = \chi^{(2)}_{YYX}$, where X corresponds to the main orientation of the collagen fibrils in the imaging plane. Thus we set: $\rho = \chi^{(2)}_{XXX}/\chi^{(2)}_{XYY}$ and we obtain:

$$I_{SHG}(\alpha) \propto I_{\text{inc}}^2 \left|\chi^{(2)}_{XYY}\right|^2 \left(\left[\rho\cos^2(\alpha-\alpha_0) + \sin^2(\alpha-\alpha_0)\right]^2 + \left[\sin 2(\alpha-\alpha_0)\right]^2\right) \tag{18}$$

Here I_{inc} is the intensity of the laser excitation. I_{SHG} shows 2 peaks and 2 minima in the range [0-180°] and ρ corresponds to the square root of the ratio of the 2 minima: $\rho = \sqrt{I(\alpha_0)/I(\alpha_0+\pi/2)}$ (see theoretical curve in Fig. 2.d and Sup. Fig. S1).

In the specific case of well-aligned fibrils with out-of-plane orientation ψ, Eq. 12 shows that $\chi^{(2)}_{XXX}$ and $\chi^{(2)}_{XYY}$ are both proportional to $\cos\psi$. As a consequence, I_{SHG} is proportional to $\cos^2\psi$: the SHG signal decreases as the out-of-plane orientation increases[11,12].

Importantly, Eq. 18 does not hold for more complex tissues, such as disordered assemblies of collagen fibrils oriented out of the imaging plane. In the latter case, there are additional terms and the parameter ρ has no direct physical interpretation.

III. P-SHG MICROSCOPY SETUP AND DATA PROCESSING

A. Experimental setup

Multiphoton imaging was performed using a custom-built laser scanning upright microscope as previously described[34] (Fig. 2.a). Briefly, the excitation source is a femtosecond

Ti-Sa laser tuned to 860 nm and scanned in the X_0Y_0 directions using galvanometric mirror. It is focused by a 10x air objective (TL10X-2P, LWD Super Apochromat, Thorlabs) with a high working distance: WD=7.77 mm to guarantee non-contact imaging even for not perfectly plane parchments, and a medium numerical aperture: NA=0.5 to enable analyses in the plane wave approximation. The resolution (FWHM) was measured as 0.7 µm in the lateral direction and 5.8 µm in the axial direction[35] and the full field of view was 750 x 750 µm^2. The excitation power at the objective focus was adjusted between 10 and 30 mW. We checked that no degradation of the parchments was induced under these conditions by verifying the reproducibility of the SHG measurements in a set of images recorded sequentially in the same area. SHG and 2PEF signals were epi-detected by photon-counting photomultiplier tubes (P25PC, Sentech) using dichroic mirrors (695DCXRU, Chroma and FF458-Fi01, Semrock) and appropriate spectral filters (FF01-680/SP and FF01-427/10, Semrock, for the SHG signal).

First, Z-stacks of *en face* SHG images were recorded with circularly polarized excitation, using 200 kHz pixel rate, 0.78 × 0.78 µm^2 pixel size and 1 µm z-step over 20 to 70 µm depth. Transverse reslices were then numerically processed (Fig. 2.b). In the following, these SHG images are displayed using a green look-up table and correspond to maximum intensity projections of the Z-stack for *en face* images or along a transverse direction for transverse reslices.

Secondly, P-SHG imaging was performed by controlling the orientation of the linear polarization of the incident laser beam by two motorized achromatic waveplates at the back pupil of the objective (Fig. 2.a). First, a quarter waveplate (MRAC2/40070707M, Fichou, France) was used to compensate for any ellipticity introduced by the microscope optical components and obtain a well-defined linear polarization: the resulting ellipticity, defined as the ratio of the minimal to maximal electric fields, was less than 3% in a central reduced field of view (FOV) of 351 × 351 µm^2. Second, a half waveplate (MRAC2/20070707M, Fichou, France) was used to rotate this linear polarization from 0° to 170° using 10° steps. A P-SHG image stack was recorded in the reduced FOV at every depth Z using these 18 incident polarizations. The pixel rate and voxel size were the same as for SHG imaging with circularly polarized excitation.

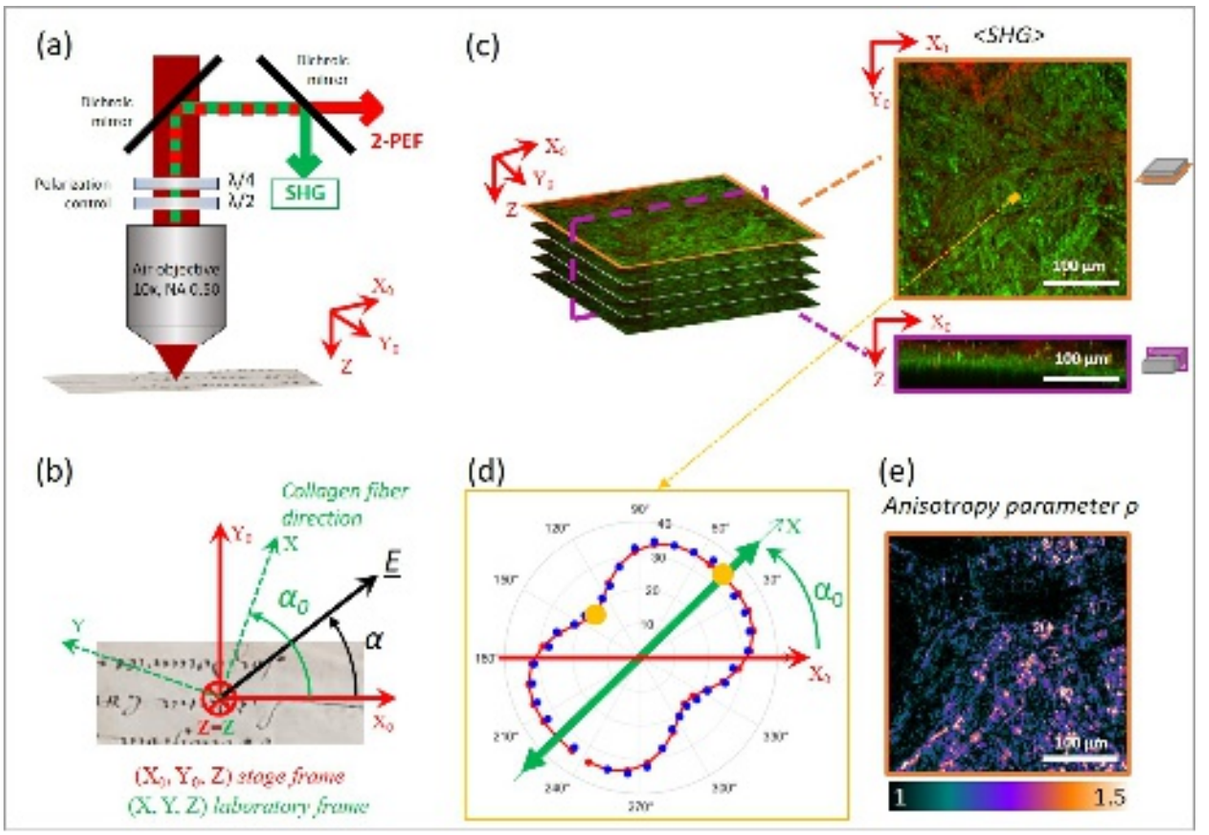

FIG. 2. P-SHG microscopy. (a) Scheme of the P-SHG set-up showing simultaneous epi-detection of the SHG and 2PEF signals by use of dichroic mirrors. The polarization state of the laser excitation is controlled by a quarter waveplate and a half waveplate. (b) Schema of the stage frame (X_0, Y_0, Z), where X_0 is the reference axis for the incident linear polarization and corresponds to the X_0 axis of the microscope stage, and of the laboratory frame (X, Y, Z) where the axis X corresponds to the direction of the collagen fiber in the imaging plane. α_0 is the angle of the collagen fiber to the stage axis X_0, while α is the angle of the incident laser polarization to the stage axis X_0. (c) Z-stack of X_0Y_0 *en face* $\langle SHG \rangle$ images. The X_0Z image is a transverse reslice. Every X_0Y_0 $\langle SHG \rangle$ image is obtained as the average of 18 images acquired at different polarization angles of the laser excitation, ranging from 0° to 170° every 10°. (d) Polarimetric diagram showing the variation of the SHG signal in the orange ROI in (c) as a function of the laser polarization angle: the main direction corresponds to the orientation of the collagen fibril and the square-root of the ratio of the two minima (orange dots) corresponds to the anisotropy parameter ρ. (e) Map of the anisotropy parameter ρ processed in every pixel of the P-SHG stack in (c).

B. P-SHG data processing

Equation (18) can be expressed as a function of its Fourier components to facilitate the processing of the P-SHG data[4]:

$$I_{SHG}(\alpha) = a_0 + a_2 \cos\left[2(\alpha - \alpha_0)\right] + a_4 \cos\left[4(\alpha - \alpha_0)\right] \tag{19}$$

where:

$$\begin{aligned} a_0 &= \frac{K}{2}\left(\frac{3\rho^2}{4} + \frac{\rho}{2} + 2\right) \\ a_2 &= 2K\left(\frac{\rho - 1}{2}\right)\left(\frac{\rho + 1}{2}\right) \\ a_4 &= \frac{K}{2}\left(\frac{\rho - 3}{2}\right)\left(\frac{\rho + 1}{2}\right) \end{aligned} \tag{20}$$

K is a constant related to I_{inc}^2, $\left|\chi_{XYY}^{(2)}\right|^2$ and other experimental parameters. The parameter ρ is then obtained as:

$$\rho = \sqrt{\frac{a_0 + a_2 + a_4}{a_0 - a_2 + a_4}} \tag{21}$$

In order to process our experimental data in a faster way, we use a Fast Fourier Transform (FFT). Eq. 19 is thus rewritten using complex coefficients:

$$I_{SHG}(\alpha) = A_0 + \left(A_2 e^{2i\alpha} + A_4 e^{4i\alpha} + cc\right) \tag{22}$$

Here $|A_0| = |a_0|$, $|A_2| = |a_2|$ and $|A_4| = |a_4|$ and the phases of A_2 and A_4 are related to the fibril orientation α_0. Our FFT image-processing workflow in Matlab (MathWorks Inc.) thus provides 4 types of information in each pixel:

- The SHG signal averaged over all incident polarization angles α: $\langle SHG \rangle = \langle I_{\text{SHG}} \rangle = |A_0|$. This $\langle SHG \rangle$ image is similar to the usual SHG image acquired with circularly polarized excitation and the same total acquisition time. For the sake of simplicity, it is only noted SHG in the following.

- The orientation α_0 of the collagen fibrils in the imaging plane. It is calculated from the phases of A_2 and A_4[21]:

$$\alpha_0 = \eta\frac{-arg(A_2)}{2} + (1 - \eta)\frac{-(arg(A_4) + \pi)}{4} \quad \text{with} \quad \eta = \frac{|A_2|^2}{|A_2|^2 + 4\,|A_4|^2} \tag{23}$$

- The anisotropy parameter ρ that is calculated as:

$$\rho = \sqrt{\frac{|A_0| + 2\,|A_2| - 2\,|A_4|}{|A_0| - 2\,|A_2| - 2\,|A_4|}} \tag{24}$$

  The minus sign before A_4 is due to the fact that a_4 is negative as $\rho < 3$ (it also explains the π shift of $arg(A_4)$ in Eq. 23). There is a positive sign before A_2 because a_2 is positive as $\rho > 1$.

- The coefficient of determination R^2 that compares in each voxel the experimental data and the data obtained when inserting the FFT parameters $|A_0|$, $|A_2|$, $|A_4|$ and α_0 into Eq. 22. Indeed, the FFT analysis provides A_0, A_2 and A_4 coefficients even if the experimental data do not match the theoretical equation (22) at all. In the latter case, there are higher order coefficients such as A_6, A_8, etc... and R^2 is low. Higher R^2 could be obtained by including the susceptibility component $\chi^{(2)}_{YYY}$ in the calculation of Eq. 16 to account for fibril assemblies that do not exhibit cylindrical symmetry as in Eq. 9.[36–39] However, we focus in this study on model collagen assemblies with cylindrical symmetries, which is obtained by eliminating voxels with low R^2 in our approach without $\chi^{(2)}_{YYY}$.

The precision of these measurements is related to the total number of detected photons[21]. We first apply a 2×2 binning filter to all images to improve the signal to noise ratio, so that the precision is around 0.05 for ρ in our experimental conditions.

C. Quantitative data analysis

The parameter R^2 is used to determine the pixels considered as valid for subsequent quantitative analyses: pixels with $R^2 < 0.7$ are filtered out and depicted as black pixels in the images. We thus obtain R^2-filtered maps of $\langle SHG \rangle$, α_0 and ρ at every depth Z.

We first perform a global quantitative analysis of the ρ parameter. The percentage of valid pixels (*i.e.* pixels with $R^2 > 0.7$) is calculated at every depth Z and a threshold is set at 10% and used to select valid Z-planes. The ρ parameter is then analyzed as follows: (i) the values of ρ are averaged over the valid pixels at every valid depth Z; (ii) these averaged values are averaged over all valid Z-planes to obtain a mean value and a standard deviation of ρ in the Region Of Interest (ROI) under study. The standard deviation is calculated the

same way. Several ROIs can be studied in the same parchment. This quantitative analysis is performed using homemade routines written in Matlab or ImageJ.

The ρ parameter is also analyzed locally in selected fibers of interest 3D renderings. Instance segmentation of fibers is automatically performed using the following Python pipeline: application of a median filter ($\sigma_{filter} = 3$), Otsu thresholding, sphere binary erosion, masked Voronoi labelling, and removing of small labels using CLIJ via pyclesperanto-prototype Python library[40] (Fig. Sup S3). The mean value and standard deviation of ρ are calculated on the mask of selected fibers of interest using regionprops from skimage Python library[41]. The out-of-imaging-plane angle ψ of every fiber is then calculated by using coordinate points placed by hand on the Z upper and lowest pixels in the fiber using Napari point layer[42]. The measurement error is estimated to be roughly 10°.

IV. IMAGING OF PARCHMENTS

A. Parchments

Two parchments are used in this study and imaged on the flesh side, the grain side or both. The first one is a goat parchment, which was crafted in 2020 by one of the authors (L. Robinet). Two types of finishing treatments were applied in two different areas on the flesh side (Sup. Fig. S2.a). The area that was just scrapped while the skin was wet is called *Scrapped*, and the area that received chalk as the parchment was wet and sanded once dry is called *Chalk and sanded*. For each finishing treatment, three samples of 1×2 cm^2 were collected. Each sample was imaged in four different ROIs on the flesh side. In total, 4×3=12 Z-stacks of P-SHG images were thus recorded for each finishing treatment (Sup Table T1).

The second parchment under study is an ancient sheep parchment dating from 1816 (Sup. Fig. S2.b). Three samples of 1×2 cm^2 were collected, one was kept as a reference (reference, D0), whilst the two others were artificially aged by heat in an oven at 100°C for 14 days (D14) and 32 days (D32). For each side of the 3 samples, four Z-stacks of P-SHG images were recorded in different ROIs. In total, 4×2=8 Z-stacks of P-SHG images were thus recorded for each of the 3 heat exposure durations (Sup Table T2). Each sample was analysed by Differential Scanning Calorimetry (DSC) to assess the degradation state of the collagen by the measurement of the shrinkage temperature (Ts)[43]. Parchment pieces of 1

mm^2 were soaked in water for 1 h, sealed in an 30 μL aluminium capsule and heated from 5°C to 120°C at 10°C/min on a Perkin Elmer DSC 8000. The measurements was repeated three times for each sample and averaged.

The parchment samples were placed under the objective of the microscope and maintained flat using lead weights (Sup. Fig. S2.c). The multiphoton analyses were non contact, non destructive and carried out without any labeling.

B. P-SHG imaging of in-plane versus out-of-plane fibers

To study experimentally the variation of the anisotropy parameter ρ in an assembly of out-of-plane fibrils versus an assembly of in-plane fibrils, we choose to use the modern goat parchment because the two different finishing treatments on the flesh side result in different organizations of the collagen fibers at the parchment surface on a macroscopic scale. The *Scrapped* area surface is smooth and flat compared to the *Chalk and sanded* area, where collagen fibers are oriented out of the sample plane with various angles, as clearly observed in white-light side images of the sample section (Fig. 3.a-b).

Figs. 3.c-f display SHG images of the two types of parchment that correspond to XZ and XY projections of *en face* Z-stacks. All SHG images show long and straight structures attributed to collagen fibers, as previously reported[24,34]. *En face* SHG image of the *Scrapped* area (Fig. 3.e) shows disordered collagen fibers with homogeneous distribution, and the transverse reslice shows that all the fibers lie within the imaging plane (Fig. 3.c). In contrast, *en face* SHG image of the *Chalk and sanded* area (Fig. 3.f) shows a less homogeneous collagen distribution and the transverse reslice shows that some fibers are spread out of the imaging plane with random orientations (Fig. 3.d).

Figs. 3.g-h display maps of the anisotropy parameter in a reduced FOV (dotted yellow square in Figs. 3.e-f), and at a specific Z depth (dotted yellow line in Figs. 3.c-d). The Z plane chosen for the *Scrapped* sample is the one with the highest SHG signal. For the *Chalk and sanded* sample, the Z plane is selected to view a maximum number of out-of-plane fibers, which corresponds to a higher Z position than for the *Scrapped* sample. We observe that ρ is larger in the *Chalk and sanded* map (in Fig. 3.h) than in the *Scrapped* one (Fig. 3.g).

This observation is quantified by calculating the average values of ρ in every Z-stack of P-SHG data. The results for the two types of sample are quite reproducible for all ROIs

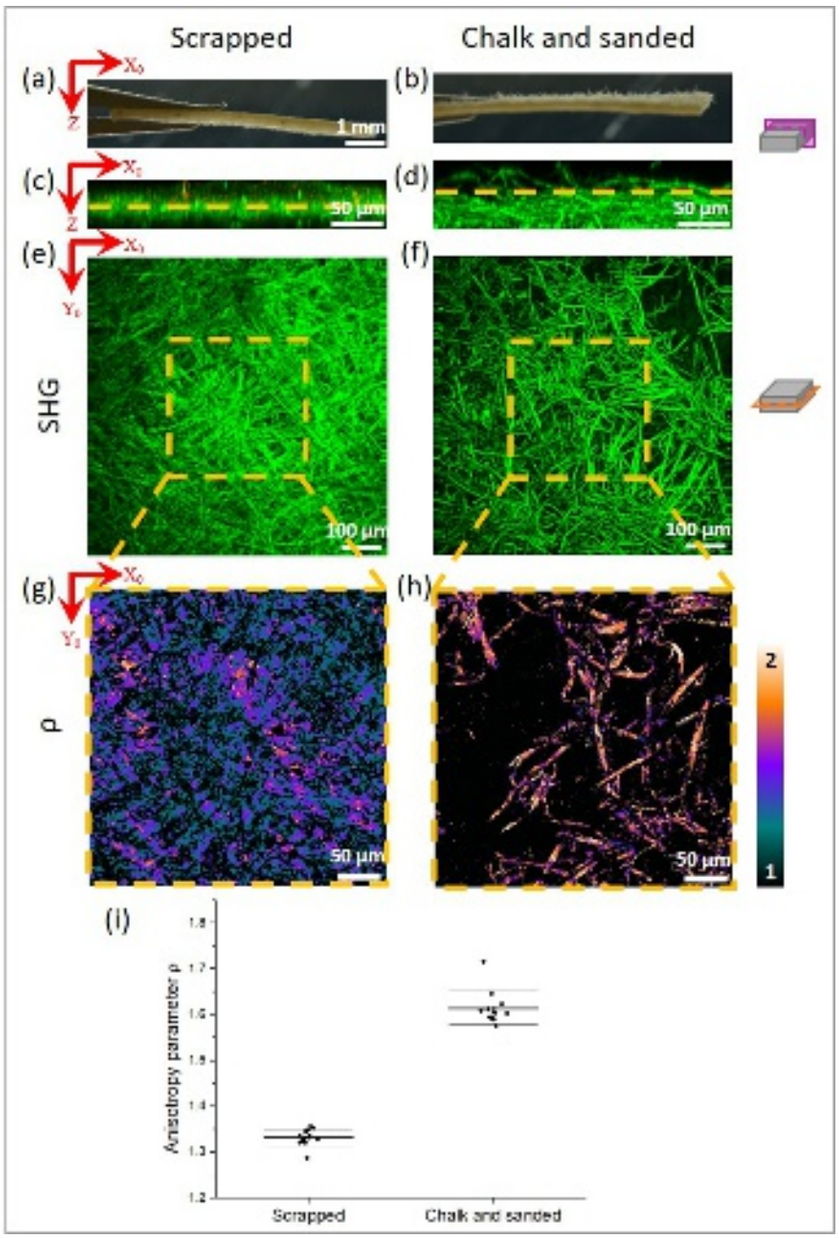

FIG. 3. SHG and P-SHG imaging of *Scrapped* and *Chalk and sanded* areas from the same parchment. (a,b) White-light image from the side of (a) the *Scrapped* sample and (b) the *Chalk and sanded* one. (c-d) Transverse reslice of SHG images (with projection along Y_0) and (e,f) *en face* SHG images (with projection along Z) of (c,e) the Scrapped sample and (d,f) the Chalk and sanded one. (g,h) Maps of the anisotropy parameter ρ of (g) the *Scrapped* sample and (h) the *Chalk and sanded* one, obtained from P-SHG imaging at the depth Z indicated by a dotted yellow line in (c,d) and in a reduced field of view delineated by yellow dotted square in (e,f). The look-up table is indicated on the right. (i) Averaged ρ data in the 12 ROIs under study of the *Scrapped* and the *Chalk and sanded* samples. The thickest line represents the mean of these data and the thinner line is the associated standard deviation.

under study (12 ROIs per type of sample), as displayed in Fig.3.i and listed in Sup Table T1. We obtain: $\rho_{\text{Scrapped}} = 1.33 \pm 0.02$ and $\rho_{\text{Chalk \& sanded}} = 1.61 \pm 0.04$. It confirms that the presence of the out-of-plane fibers in the *Chalk and sanded* sample results in a larger anisotropy parameter ρ than in the *Scrapped* sample that contains only in-plane fibers, in agreement with our theoretical calculation (Eq. 13).

As the *Chalk and sanded* sample contains both in-plane and out-of-plane fibers (Fig.3.d), a more accurate approach consists in a local analysis of the anisotropy parameter ρ and the out-of-plane orientation ψ of these two types of fibers. For that purpose, we use a transverse reslice of a P-SHG image with a large Z range in order to visualize out-of-plane fibers over their full length (Fig. 4.a). In-plane fibers are also easily identified as they are grouped at the bottom of the SHG image. When selecting an out-of-plane fiber within a transverse plane, the associated anisotropy parameter map shows clearly that ρ is higher in this fiber than in the fibers parallel to the imaging plane (Fig. 4.b). Connected Component Analysis in Python then allows processing of local averages of ρ in fibers or group of fibers, which can be plotted as a function of the out-of-plane angle ψ measured by use of the coordinates of the voxels at the two fiber ends. Fig. 4.c displays these 8 measurements, where the ψ angle varies from 10° to 25° with an estimated measurement error of 10°. They are superimposed on the theoretical behavior of $\rho_{opt}^{out}(\psi)$ given by Eq. 13, where ρ_{fib} is set to 1.36[8,44] as in previous reports or to 1.48 that is the average measurement in the in-plane fibers of this sample. A good agreement is observed between the experimental measurements and the theoretical curves.

C. P-SHG imaging of disordered fibril assemblies

Let's now address the variation of ρ as a function of disorder. For this study, series of samples were artificially aged by heat exposure to mimic collagen degradation through oxidation.[23] If the collagen is in an advanced stage of degradation, it eventually leads to the denaturation of collagen into gelatin that is the unfolding of the collagen triple-helical structure at molecular scale. In this extreme case, no more SHG signals is detected due to the loss of the hierarchical organization.[34] However, early steps of degradation only correspond to a disorganization of the collagen structure that preserves the fiber distribution.[23,34]

The state of degradation of collagen in parchments is first characterized by means of

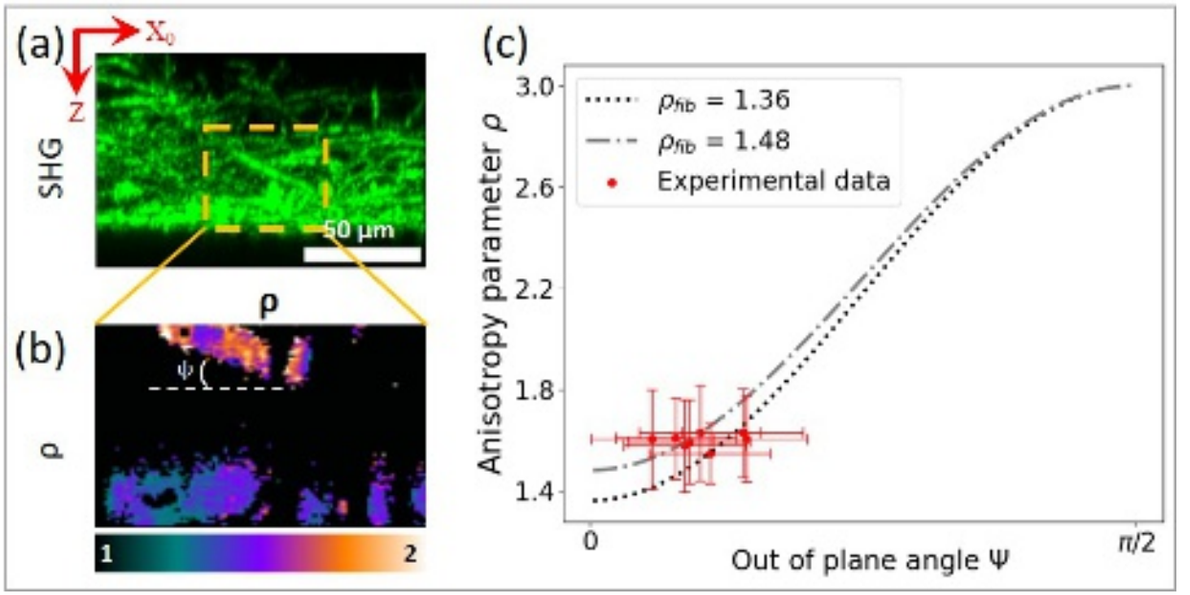

FIG. 4. Variation of ρ with the collagen out-of-plane orientation. (a) Transverse reslice of SHG image (projection along Y_0). (b) Anisotropy parameter map at a specific Y_0 in the region delimited by the orange dotted rectangle in (a). (c) Theoretical variation of the anisotropy parameter ρ as a function of the out-of-plane angle ψ according to Eq. 13, starting from two different values of ρ_{fib}. Experimental data obtained from 8 out-of-plane fibers as in (b) are superimposed in red color.

DSC measurements in every sample. As expected, the three samples under study exhibit a decreasing shrinkage temperature T_s for increasing heat aging duration: $51.5°C \pm 2.8°C$ for the reference sample D0, $38.1°C \pm 0.2°C$ for the D14 sample and $35.3°C \pm 3.1°C$ for the D32 sample (Sup Table T2). It is attributed to a progressive disorganization of collagen when the duration of the heat exposure increases, as already observed in previous studies.[23,34] This disorganization is expected to include an orientation disorder in the fibril assembly within fibers as depicted in Fig. 1.f. and a disorder in the molecular packing within every fibril.[45]

P-SHG stacks recorded on the grain and flesh sides of each sample are displayed in Fig. 5. SHG images of the D0 and D32 samples show similar distribution of the collagen fibers at the millimeter scale (Figs. 5.a,c, projections of the Z- stacks). Note however that the SHG signal decreases from D0 to D32, as already reported[34], which is not visible here because the look-up table is defined arbitrarily for every sample. This decrease is consistent with a loss of collagen order at submicrometer scale. The associated ρ maps at a specific Z plane and in the same ROIs show larger values for the D32 sample than for the D0 sample (Figs. 5.b, d).

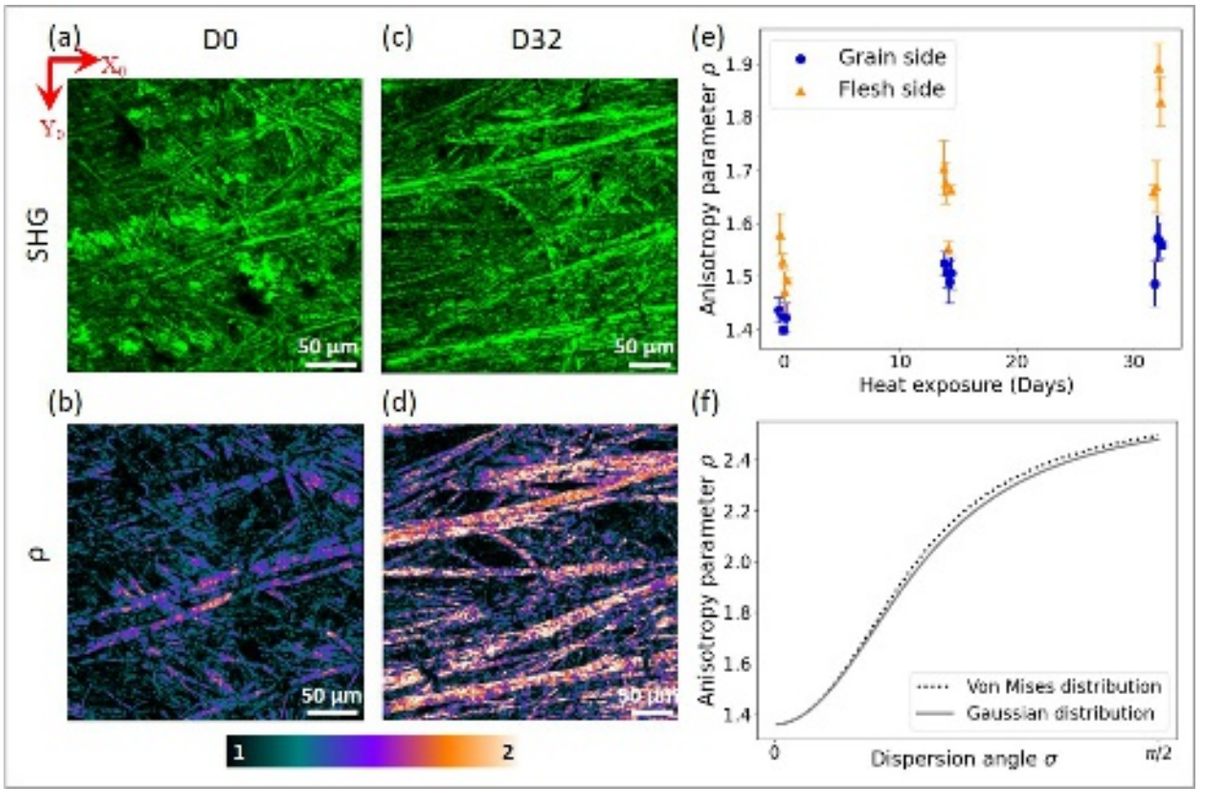

FIG. 5. Variation of ρ with collagen disorder. (a, c) *En face* SHG images (projection along Z) and (b, d) ρ maps (single Z plane) of (a,b) the reference sample D0 and (c,d) the aged-one D32 . The SHG look-up table is arbitrary. The ρ look-up table is depicted in the bottom. (e) Experimental measurements of ρ on the flesh side (blue dots) and the grain side (orange triangles) as a function of the heat exposure duration. (f) Theoretical variation of ρ as a function of the variance σ of the orientational disorder of the fibrils. Eq. 15 is plotted for Von Mises (dotted line) and Gaussian (solid line) distributions.

The same behavior is observed in all P-SHG stacks on both the flesh and grain sides (4 ROIs per condition), as displayed in Fig. 5.e and listed in Sup Table T2. It is consistent with the theoretical variation of ρ as a function of disorder that is expressed in Eq. 15 and plotted in Fig. 5.f. ρ increases from the ρ_{fib} value to 2.50 for a Van Mises distribution or 2.48 for a Gaussian one, when the variance σ of the fibril orientation distribution increases. As this theoretical calculation also applies to an orientation disorder of collagen molecules within a single fibril, we attribute the increase of ρ in the degraded parchments to an increase of disorder at sub-micrometer scale.

V. DISCUSSION

In this paper, we have developed a comprehensive study of the variation of the anisotropy parameter ρ in P-SHG microscopy of collagen. This parameter quantifies the contrast of the polarimetric SHG signal in collagen tissues: it is equal to the squareroot of the ratio of the SHG signal for incident linear polarization parallel to the collagen fiber to that for incident polarization perpendicular to the fiber.

First, we have performed a theoretical multiscale analysis of the variation of ρ as a function of the distribution of the collagen fibrils within the focal volume. We have obtained analytical expressions valid for any collagen distribution and then considered three model distributions leading to simplified equations: (i) assembly of aligned fibrils within the imaging plane, (ii) assembly of aligned fibrils oriented out of the imaging plane, (iii) assembly of disordered fibrils within the imaging plane (Fig.1). Our calculations show that the anisotropy parameter ρ increases when the out-of-plane angle or the disorder increase, starting from its value around 1.4 for a unique fibril lying within the imaging plane up to 3 for out-of-plane fibrils or around 2.5 for disordered fibrils. Our analytical approach shows two main limitations: (i) it is performed in the plane wave approximation, while moderate to strong focusing is used in SHG microscopy, (ii) it only considers model collagen distributions that do not reflect the complexity of collagen organization in tissues. To address these two limitations, more advanced numerical approaches can be developed, for instance using Green function formalism and modeling complex 3D geometries of collagen[19,46]. It would enable to consider assemblies of fibrils with different sizes that cross at any angle and exhibit a super-helical structure[32,38,46]. However, the advantage of our analytical approach with model distributions is to provide simple expressions that can be used in a straightforward way to analyze experimental data and get insight into the collagen structure. Moreover, as discussed below, we obtain a good agreement with experimental P-SHG imaging of parchment with a 0.5 NA air objective, which shows that the plane wave approximation provide reliable results for moderate focusing.

Secondly, we have performed P-SHG microscopy experiments in parchments in order to verify the predictions of our theoretical calculations. Parchments are relevant collagen materials for this study because they are obtained from animal skins that have been dried under tension after removal of mainly hair and fat. Parchments are therefore mainly composed of

stretched collagen fibers parallel to the parchment surface, that is parallel to the imaging plane. These fibers are thus appropriate models for tight assembly of aligned in-plane fibrils. Moreover, specific finishing treatment with chalk and pumice, performed to remove remaining fat and to have a white and opaque surface suitable for writing, can result in the presence of out-of-plane oriented fibers at the surface of the parchment. These type of parchments are then appropriate models for tight assembly of aligned *out-of-plane* fibrils. Finally, early steps of degradation by heat have been shown to induce disorder in the fiber structure, so that heat-degraded parchments are appropriate models for assembly of *disordered* in-plane fibrils[34]. Advantageously, tight assemblies of aligned in-plane and out-of-plane fibrils are obtained from the same parchment, which is separated in two regions subjected to two different finishing treatments. Similarly, several samples are collected in the same parchment and exposed to heat for different durations. Each of these 2 series of p-SHG measurements is thus performed in a unique parchment, which ensures reliable comparison with the reference measurement of in-plane aligned fibrils. Indeed, ρ measurements may result in different values from one parchment to the other because of the variability of the animal skins from which they are made and of the differences in the parchment manufacturing.

Our theoretical calculations and experimental P-SHG data exhibit a good agreement. It demonstrates that an increase of the anisotropy parameter ρ can be attributed to an increase of the disorder or of the out-of-plane angle and that in both cases, ρ is affected with the same order of magnitude. It may thus be difficult to discriminate between disorder and out-of-plane orientation, both in thin sections and in dense tissues, where transverse reslices do not enable the visualization of the fiber out-of-plane orientation. However, in most tissues, this out-of-plane orientation can be characterized in transverse reslice or 3D rendering, so that an increase in ρ can be attributed to disorder or not in a reliable way. It is notably the case in parchments that exhibit only in-plane fibers[34].

VI. CONCLUSION

This study aimed at implementing a comprehensive study of the variation of the anisotropy parameter ρ, which quantifies the polarimetric contrast in P-SHG microscopy of collagen. We developped an analytical multiscale approach of collagen P-SHG and demonstrated that the anisotropy parameter ρ increases when the disorder or the out-of-plane

angle increases. These theoretical calculations were confirmed by P-SHG experiments in series of parchments samples exhibiting different geometries of collagen fibers. Our study therefore provides an efficient way to attribute a variation of ρ to a variation of the collagen distribution and to get insight into the collagen structure in different tissues. It may be generalized to other proteins assemblies that exhibit SHG signal, such as myosin and tubulin, although it would require to take into account the specific structure of these proteins[16].

VII. SUPPLEMENTARY MATERIAL

Supplementary Figure S1: P-SHG imaging and processing.

Supplementary Figure S2: Parchments under study.

Supplementary Figure S3: Processing pipeline of out-of-plane fiber images.

Supplementary Table 1: P-SHG data for the handmade goat parchment with different finishing treatments.

Supplementary Table 2: P-SHG data for the ancient sheep parchment. Artificial aging was induced by heat exposure (100°C) during 0 (reference), 14 and 32 days.

ACKNOWLEDGMENTS

GG, GL, CC and MCSK thank Xavier Solinas and Jean-Marc Sintès for technical support in the SHG setup and Nicolas Olivier and the "Advanced microscopy and tissue physiology" group at LOB for fruitful discussions. LR thanks Jiří Vnouček for the training on the parchment manufacturing and Olivier Deparis and the university of Namur for the organisation of the parchment manufacturing workshop in september 2020.

GG, GL, CC and MCSK acknowledge fundings from the French "Agence Nationale de la Recherche" (ANR-10-INBS-04, ANR-11-EQPX-0029, ANR-21-ESRE-0050). GG is funded by the MITI-CNRS.

AUTHOR DECLARATION

Conflict of Interest

The authors have no conflicts to disclose.

Author Contributions

Giulia Galante: Formal Analysis (equal); Investigation (lead); Software (equal); Writing/Original Draft Preparation (equal) **Laurianne Robinet**: Conceptualization (equal); Funding Acquisition(equal); Methodology (equal); Supervision (equal); Validation (equal); Writing/Review & Editing (equal); **Sylvie Heu-Thao**: Investigation (supporting); Methodology (equal); Writing/Review & Editing (equal); **Clément Caporal**: Methodology (equal); Software (equal); Writing/Review & Editing (equal); **Gaël Latour**: Conceptualization (equal); Funding Acquisition(equal); Methodology (equal); Supervision (equal); Validation (equal); Writing/Review & Editing (equal); **Marie-Claire Schanne-Klein**: Conceptualization (lead); Funding Acquisition (equal); Methodology (equal); Supervision (equal); Validation (equal); Writing/Original Draft Preparation (lead)

DATA AVAILABILITY STATEMENT

Data underlying the results presented in this paper are not publicly available at this time but may be obtained from the corresponding author upon reasonable request.

REFERENCES

[1]D. Hulmes, "Building collagen molecules, fibrils, and suprafibrillar structures," J. Struct. Biol. **137**, 2–10 (2002).

[2]X. Y. Chen, O. Nadiarynkh, S. Plotnikov, and P. J. Campagnola, "Second harmonic generation microscopy for quantitative analysis of collagen fibrillar structure," Nat. Protocols **7**, 654–669 (2012).

[3]S. Bancelin, C. Aimé, I. Gusachenko, L. Kowalczuk, G. Latour, T. Coradin, and M.-C. Schanne-Klein, "Determination of collagen fibril size via absolute measurements of second-harmonic generation signals," Nat. Commun. **5**, 4920 (2014).

[4]P. Stoller, K. Reiser, P. Celliers, and A. Rubenchik, "Polarization-modulated second harmonic generation in collagen," Biophys J. **82**, 3330–3342 (2002).

[5]F. Tiaho, G. Recher, and D. Rouède, "Estimation of helical angle of myosin and collagen by second harmonic generation imaging microscopy," Opt. Express **15**, 12286–12295 (2007).

[6]J. C. Mansfield, C. P. Winlove, J. Moger, and S. J. Matcher, "Collagen fiber arrangement in normal and diseased cartilage studied by polarization sensitive nonlinear microscopy," J. Biomed. Optics **13**, 044020 (2008).

[7]I. Gusachenko, G. Latour, and M.-C. Schanne-Klein, "Polarization-resolved second harmonic microscopy in anisotropic thick tissues," Opt. Express **18**, 19339–19352 (2010).

[8]I. Gusachenko, Y. Goulam Houssen, V. Tran, J.-M. Allain, and M.-C. Schanne-Klein, "Polarization-resolved second-harmonic microscopy in tendon upon mechanical stretching," Biophys. J. **102**, 2220–2229 (2012).

[9]J. Duboisset, D. Ait-Belkacem, M. Roche, H. Rigneault, and S. Brasselet, "Generic model of the molecular orientational distribution probed by polarization-resolved second-harmonic generation," Phys. Rev. A **85** (2012), Artn 043829 Doi 10.1103/Physreva.85.043829.

[10]A. E. Tuer, M. K. Akens, S. Krouglov, D. Sandkuijl, B. C. Wilson, C. M. Whyne, and V. Barzda, "Hierarchical model of fibrillar collagen organization for interpreting the second-order susceptibility tensors in biological tissue," Biophys. J. **103**, 2093–2105 (2012).

[11]S. Psilodimitrakopoulos, I. Amat-Roldan, P. Loza-Alvarez, and D. Artigas, "Effect of molecular organization on the image histograms of polarization shg microscopy," Biomed Opt Express **3**, 2681–2693 (2012).

[12]C. Teulon, A. Tidu, F. Portier, G. Mosser, and M.-C. Schanne-Klein, "Probing the 3d structure of cornea-like collagen liquid crystals with polarization-resolved shg microscopy," Opt. Express **24**, 16084–16098 (2016).

[13]D. Rouede, E. Schaub, J. J. Bellanger, F. Ezan, J. C. Scimeca, G. Baffet, and F. Tiaho, "Determination of extracellular matrix collagen fibril architectures and pathological remodeling by polarization dependent second harmonic microscopy," Sci. Rep. **7** (2017), ARTN 12197 10.1038/s41598-017-12398-0.

[14]E. I. Romijn, A. Finnoy, and M. B. Lilledahl, "Analyzing the feasibility of discriminating between collagen types i and ii using polarization-resolved second harmonic generation," J Biophot **12** (2019), 10.1002/jbio.201800090.

[15]M. Harvey, R. Cisek, D. Tokarz, and L. Kreplak, "Effect of out of plane orientation on polarization second harmonic generation of single collagen fibrils," Biomed Opt Express **14**, 6271–6282 (2023).

[16]B. Asadipour, E. Beaurepaire, X. Zhang, A. Chessel, P. Mahou, W. Supatto, M.-C. Schanne-Klein, and C. Stringari, "Modelling and predicting second harmonic generation from protein molecular structure," Phys. Rev. X **14**, 011038 (2024).

[17]S. V. Plotnikov, A. Millard, P. Campagnola, and W. Mohler, "Characterization of the myosin-based source for second-harmonic generation from muscle sarcomeres," Biophys. J. **90**, 693–703 (2006).

[18]D. Aït-Belkacem, A. Gasecka, F. Munhoz, S. Brustlein, and S. Brasselet, "Influence of birefringence on polarization resolved nonlinear microscopy and collagen shg structural imaging," Opt. Express **18**, 14859–14870 (2010).

[19]I. Gusachenko and M.-C. Schanne-Klein, "Numerical simulation of polarization-resolved second harmonic microscopy in birefringent media," Phys. Rev. A **88**, 053811 (2013).

[20]C. Teulon, I. Gusachenko, G. Latour, and M.-C. Schanne-Klein, "Theoretical, numerical and experimental study of geometrical parameters that affect anisotropy measurements in polarization-resolved shg microscopy," Opt. Express **23**, 9313–9328 (2015).

[21]V. Wasik, P. Refregier, M. Roche, and S. Brasselet, "Precision of polarization-resolved second harmonic generation microscopy limited by photon noise for samples with cylindrical symmetry," J. Opt. Soc. Am. A **32**, 1437–1445 (2015).

[22]D. Rouede, J. J. Bellanger, J. Bomo, G. Baffet, and F. Tiaho, "Linear least square (lls) method for pixel-resolution analysis of polarization dependent shg images of collagen fibrils," Opt Express **23**, 13309–19 (2015).

[23]R. Larsen, "Improved assessment of parchment (IDAP). assessment, data collection and sharing of knowledge," Luxembourg, European Commission: (2007).

[24]G. Latour, L. Robinet, A. Dazzi, F. Portier, A. Deniset-Besseau, and M.-C. Schanne-Klein, "Correlative nonlinear optical microscopy and infrared nanoscopy reveals collagen degradation in altered parchments," Sci. Rep. **6**, 36344 (2016).

[25]J. Duboisset, A. Deniset-Besseau, E. Benichou, I. Russier-Antoine, N. Lascoux, C. Jonin, F. Hache, M.-C. Schanne-Klein, and P.-F. Brevet, "A bottom-up approach to build the hyperpolarizability of peptides and proteins from their amino-acids," J. Phys. Chem. B **117**, 9877–9881 (2013).

[26]K. Beck and B. Brodsky, "Supercoiled protein motifs: the collagen triple-helix and the alpha-helical coiled coil," J Struct Biol **122**, 17–29 (1998).

[27]C. Loison and D. Simon, "Additive Model for the Second Harmonic Generation Hyperpolarizability Applied to a Collagen-Mimicking Peptide (Pro-Pro-Gly)(10)," Journal of Physical Chemistry A **114**, 7769–7779 (2010).

[28]A. E. Tuer, S. Krouglov, N. Prent, R. Cisek, D. Sandkuijl, K. Yasufuku, B. C. Wilson, and V. Barzda, "Nonlinear optical properties of type i collagen fibers studied by polarization dependent second harmonic generation microscopy," J. Phys. Chem. B **115**, 12759–12769 (2011).

[29]M. de Wergifosse, J. de Ruyck, and B. Champagne, "How the second-order nonlinear optical response of the collagen triple helix appears: A theoretical investigation," The Journal of Physical Chemistry C **118**, 8595–8602 (2014).

[30]M. Harvey, R. Cisek, M. Alizadeh, V. Barzda, L. Kreplak, and D. Tokarz, "High numerical aperture imaging allows chirality measurement in individual collagen fibrils using polarization second harmonic generation microscopy," Nanophotonics **12**, 2061–2071 (2023).

[31]J. S. Bell, S. Hayes, C. Whitford, J. Sanchez-Weatherby, O. Shebanova, N. J. Terrill, T. L. M. Sorensen, A. Elsheikh, and K. M. Meek, "Tropocollagen springs allow collagen fibrils to stretch elastically," Acta Biomater **142**, 185–193 (2022).

[32]A. I. Brown, L. Kreplak, and A. D. Rutenberg, "An equilibrium double-twist model for the radial structure of collagen fibrils," Soft Matter **10**, 8500–11 (2014).

[33]A. Deniset-Besseau, J. Duboisset, E. Benichou, F. Hache, P.-F. Brevet, and M.-C. Schanne-Klein, "Measurement of the second order hyperpolarizability of the collagen triple helix and determination of its physical origin." J. Phys. Chem. B **113**, 13437–13445 (2009).

[34]M. Schmeltz, L. Robinet, S. Heu-Thao, J. M. Sintes, C. Teulon, G. Ducourthial, P. Mahou, M. C. Schanne-Klein, and G. Latour, "Noninvasive quantitative assessment of collagen degradation in parchments by polarization-resolved SHG microscopy," Sci Adv **7** (2021), 10.1126/sciadv.abg1090.

[35]P. Mahou, G. Malkinson, E. Chaudan, T. Gacoin, E. Beaurepaire, and W. Supatto, "Metrology of multiphoton microscopes using second harmonic generation nanoprobes," Small **13** (2017), 10.1002/smll.201701442.

[36]R. Ambekar, T. Y. Lau, M. Walsh, R. Bhargava, and J. Toussaint, K. C., "Quantifying collagen structure in breast biopsies using second-harmonic generation imaging," Biomed Opt Express **3**, 2021–35 (2012).

[37]R. Mercatelli, S. Mattana, L. Capozzoli, F. Ratto, F. Rossi, R. Pini, D. Fioretto, F. S. Pavone, S. Caponi, and R. Cicchi, "Morpho-mechanics of human collagen superstructures revealed by all-optical correlative micro-spectroscopies," Commun Biol **2**, 117 (2019).

[38]H. Jeon, M. Harvey, R. Cisek, E. Bennett, and D. Tokarz, "Characterization of pathological stomach tissue using polarization-sensitive second harmonic generation microscopy," Biomed Opt Express **14**, 5376–5391 (2023).

[39]T. Zheng, E. G. Pendleton, R. P. Barrow, A. D. Maslesa, P. A. Kner, and L. J. Mortensen, "Spatial polarimetric second harmonic generation evaluation of collagen in a hypophosphatasia mouse model," Biomed Opt Express **15**, 6940–6956 (2024).

[40]R. Haase, L. A. Royer, P. Steinbach, D. Schmidt, A. Dibrov, U. Schmidt, M. Weigert, N. Maghelli, P. Tomancak, F. Jug, and E. W. Myers, "CLIJ: GPU-accelerated image processing for everyone," Nature Methods **17** (2020), 10.1038/s41592-019-0650-1.

[41]S. Van der Walt, J. L. Schönberger, J. Nunez-Iglesias, F. Boulogne, J. D. Warner, N. Yager, E. Gouillart, and T. Yu, "scikit-image: image processing in python," PeerJ **2**, e453 (2014).

[42]N. Sofroniew, T. Lambert, G. Bokota, J. Nunez-Iglesias, P. Sobolewski, A. Sweet, L. Gaifas, K. Evans, A. Burt, D. Doncila Pop, K. Yamauchi, M. Weber Mendonça, G. Buckley, W.-M. Vierdag, L. Royer, A. Can Solak, K. I. S. Harrington, J. Ahlers, D. Althviz Moré, O. Amsalem, A. Anderson, A. Annex, P. Boone, J. Bragantini, M. Bussonnier, C. Caporal, J. Eglinger, A. Eisenbarth, J. Freeman, C. Gohlke, K. Gunalan, H. Har-Gil, M. Harfouche, V. Hilsenstein, K. Hutchings, J. Lauer, G. Lichtner, Z. Liu, L. Liu, A. Lowe, L. Marconato, S. Martin, A. McGovern, L. Migas, N. Miller, H. Muñoz, J.-H. Müller, C. Nauroth-Kreß, D. Palecek, C. Pape, E. Perlman, K. Pevey, G. Peña-Castellanos, A. Pierré, D. Pinto, J. Rodríguez-Guerra, D. Ross, C. T. Russell, J. Ryan, G. Selzer, M. Smith, P. Smith, K. Sofiiuk, J. Soltwedel, D. Stansby, J. Vanaret, P. Wadhwa, M. Weigert, J. Windhager, P. Winston, and R. Zhao, "Napari: a multi-dimensional image viewer for Python," (2024).

[43]C. Chahine, "Changes in hydrothermal stability of leather and parchment with deterioration: a dsc study," Thermochimica Acta **365**, 101–110 (2000).

[44]G. Latour, I. Gusachenko, L. Kowalczuk, I. Lamarre, and M.-C. Schanne-Klein, "In vivo structural imaging of the cornea by polarization-resolved second harmonic microscopy," Biomed. Opt. Express **3**, 1 (2012).

[45]C. A. Miles and M. Ghelashvili, "Polymer-in-a-box mechanism for the thermal stabilization of collagen molecules in fibers," Biophys J **76**, 3243–52 (1999).

[46]C. P. Brown, M. A. Houle, K. Popov, M. Nicklaus, C. A. Couture, M. Laliberte, T. Brabec, A. Ruediger, A. J. Carr, A. J. Price, H. S. Gill, L. Ramunno, and F. Légaré, "Imaging and modeling collagen architecture from the nano to micro scale," Biomed. Opt. Express **5**, 233–243 (2014).